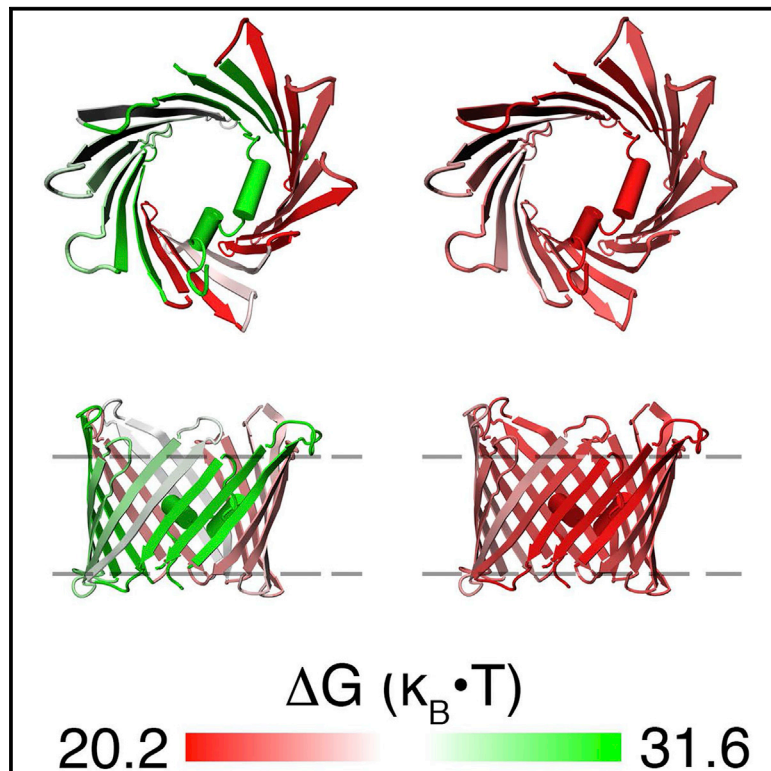


Structure

Molecular Plasticity of the Human Voltage-Dependent Anion Channel Embedded Into a Membrane

Graphical Abstract



Authors

Lin Ge, Saskia Villinger, Stefania A. Mari, ..., Stefan Becker, Daniel J. Müller, Markus Zweckstetter

Correspondence

daniel.mueller@bsse.ethz.ch (D.J.M.), markus.zweckstetter@dzne.de (M.Z.)

In Brief

VDAC is the primary gatekeeper of mitochondria. Ge et al. use single-molecule force spectroscopy in combination with NMR spectroscopy to show that the membrane-embedded barrel of human VDAC is highly flexible. Because calcium considerably decreases the pore's conformational variability, this modulation might provide the means to influence VDAC function.

Highlights

- Human VDAC1 in the membrane is structurally flexible
- The β barrel of human VDAC can stepwise unfold β hairpins
- Ca^{2+} considerably decreases the conformational variability of hVDAC1
- Ca^{2+} considerably decreases the free energy stabilizing hVDAC1



Molecular Plasticity of the Human Voltage-Dependent Anion Channel Embedded Into a Membrane

Lin Ge,^{1,5} Saskia Villinger,^{2,5} Stefania A. Mari,¹ Karin Giller,² Christian Griesinger,² Stefan Becker,² Daniel J. Müller,^{1,*} and Markus Zweckstetter^{2,3,4,*}

¹Department of Biosystems Science and Engineering, Eidgenössische Technische Hochschule (ETH) Zürich, Mattenstrasse 26, 4058 Basel, Switzerland

²Department of NMR-based Structural Biology, Max Planck Institute for Biophysical Chemistry, Am Fassberg 11, 37077 Göttingen, Germany

³Structural Biology in Dementia, German Center for Neurodegenerative Diseases (DZNE), Von-Siebold-Strasse 3a, 37075 Göttingen, Germany

⁴Department of Neurology, University Medical Center Göttingen, University of Göttingen, Am Waldweg 33, 37073 Göttingen, Germany

⁵Co-first author

*Correspondence: daniel.mueller@bsse.ethz.ch (D.J.M.), markus.zweckstetter@dzne.de (M.Z.)

<http://dx.doi.org/10.1016/j.str.2016.02.012>

SUMMARY

The voltage-dependent anion channel (VDAC) regulates the flux of metabolites and ions across the outer mitochondrial membrane. Regulation of ion flow involves conformational transitions in VDAC, but the nature of these changes has not been resolved to date. By combining single-molecule force spectroscopy with nuclear magnetic resonance spectroscopy we show that the β barrel of human VDAC embedded into a membrane is highly flexible. Its mechanical flexibility exceeds by up to one order of magnitude that determined for β strands of other membrane proteins and is largest in the N-terminal part of the β barrel. Interaction with Ca^{2+} , a key regulator of metabolism and apoptosis, considerably decreases the barrel's conformational variability and kinetic free energy in the membrane. The combined data suggest that physiological VDAC function depends on the molecular plasticity of its channel.

INTRODUCTION

VDAC is the most abundant protein in the outer mitochondrial membrane and is the only known pathway for metabolites and small ions into the mitochondrial matrix (Bathori et al., 2006; Benz, 1994; Gincel et al., 2001; Shoshan-Barmatz et al., 2010a; Tan and Colombini, 2007). VDAC has been implicated as a critical regulator of apoptosis (Shoshan-Barmatz et al., 2010b) and as a component of the Ca^{2+} -regulated permeability transition pore (Crompton, 1999; Narita et al., 1998; Szabo et al., 1993; Zoratti and Szabo, 1995). It determines metabolite flow by voltage-dependent conformational changes between a high-conductance anion-selective state and several low-conductance states favoring small cations (Blachly-Dyson and Forte, 2001; Schein et al., 1976). Although the existence of these

states is widely accepted, their molecular nature has not been resolved to date.

VDAC forms a 19-stranded β barrel with an N-terminal amphipathic α helix located inside the pore (Bayrhuber et al., 2008; Hiller et al., 2008; Ujwal et al., 2008). Electron microscopy and black lipid membrane measurements indicated that channel closure is accompanied by large structural changes (Guo and Mannella, 1993; Peng et al., 1992; Zimmerberg and Parsegian, 1986). In addition, early studies suggested that the α helix and some β strands form a voltage sensor, which moves out of the membrane and thus results in a smaller pore (Song et al., 1998; Thomas et al., 1993). In an alternative gating model, the N-terminal α helix moves into the pore lumen while the β barrel remains unchanged (Hiller and Wagner, 2009; Ujwal et al., 2008). However, both these mechanisms were recently questioned by experiments, which demonstrated functional channel gating of VDAC even after crosslinking of the α helix to the channel wall (Teijido et al., 2012). A new hypothesis then emerged, which suggested deformations of the β barrel as a possible mechanism for voltage-dependent gating of VDAC (Villinger et al., 2010; Zachariae et al., 2012).

Mitochondria possess several uptake and release mechanisms, which control the amount of calcium in the mitochondrial matrix and thereby ATP production (Gunter and Sheu, 2009; Jouaville et al., 1999; McCormack et al., 1990; Nichols and Denton, 1995; Territo et al., 2000, 2001). In addition, increasing concentrations of cytosolic Ca^{2+} can lead to calcium overload, mitochondrial membrane permeabilization, and release of proapoptotic factors (Liu et al., 1996; Susin et al., 1996). Ca^{2+} itself has been proposed to induce opening of the VDAC channel (Bathori et al., 2006), while others reported that it has no influence on channel gating (Rostovtseva et al., 2005). In addition, two Ca^{2+} -binding sites have been suggested on the basis of bilayer measurements of VDAC mutants (Israelson et al., 2007, 2008). However, direct evidence for the influence of Ca^{2+} on the molecular structure of VDAC is missing.

Here we provide insights into the molecular nature of the conformational transitions that occur in a single membrane-embedded human VDAC channel. Using single-molecule force

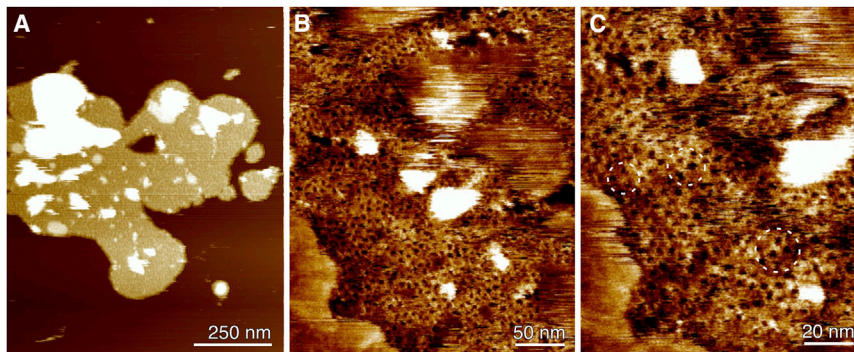


Figure 1. AFM Topographs of hVDAC1 Reconstituted into Lipid Membranes

(A) Overview showing membrane patches. (B) High-resolution topography showing the membrane surface peppered with small pores. Patches of densely packed pores are surrounded by higher protruding lipid membrane, which makes it difficult to contour hVDAC1 molecules by the AFM tip. (C) At higher resolution, the individual pores formed by hVDAC1 become better visible (dashed circles). Single-molecule force spectroscopy experiments of hVDAC1 channels were conducted on such densely packed patches.

spectroscopy in combination with nuclear magnetic resonance (NMR) spectroscopy, we show that the molecular plasticity of VDAC lies up to one order of magnitude above that determined for β strands of other transmembrane proteins. VDAC's mechanical flexibility is strongly decreased by Ca^{2+} and Mg^{2+} , suggesting that VDAC function is regulated by deformations of its channel structure.

RESULTS

Single-Molecule Force Spectroscopy of hVDAC1 in Membranes

To quantify the conformational variability within isoform 1 of human VDAC (hVDAC1), which is the primary channel protein involved in ion transport and cellular apoptosis, we recombinantly produced pure hVDAC1 and reconstituted it into lipid membranes. Using solid-state NMR spectroscopy in combination with electrophysiological measurements, we and others have previously demonstrated the structural and functional integrity of the liposome-reconstituted hVDAC1 channel (Bauer et al., 2011; Eddy et al., 2012, 2015; Schneider et al., 2010; Zachariae et al., 2012). Next, we imaged the membrane-embedded protein by atomic force microscopy (AFM) (Figure 1). The membranes had a rather smooth appearance and showed densely packed pores formed by hVDAC1. The arrangement of the pores indicates that hVDAC1 assembles into heterogeneous oligomeric forms, in agreement with previous reports and the localization of hVDAC1 in distinct domains in the outer membrane of mitochondria (Hoogenboom et al., 2007; Neumann et al., 2010). After AFM imaging, the AFM tip was pushed onto densely packed hVDAC1 assemblies to facilitate the non-specific attachment to one of the termini of an individual channel (Figure 2A). Withdrawal of the AFM tip stretched the terminus and induced stepwise unfolding of the protein resulting in a characteristic saw-tooth like force-distance (FD) curve (Figure 2B). To this end, only FD curves corresponding to the fully stretched length (>75 nm) of an unfolded hVDAC1 polypeptide were analyzed (Bippes and Muller, 2011; Oosterhelt et al., 2000). At distances >100 nm, the FD curves detected no interactions suggesting that the channel has been fully unfolded and extracted from the membrane. It has been shown that the non-specific attachment of the terminus to the AFM tip is transient and that the unfolded polypeptide slips off the tip after a few seconds (Oosterhelt et al., 2000). Thus, after a waiting time of a few seconds, the tip was ready to attach a new hVDAC1 molecule and to record the next unfolding FD curve.

The individual unfolding curves of single hVDAC1 channels revealed a series of force peaks, which varied in occurrence demonstrating that the unfolding steps have a certain probability to occur and that multiple unfolding pathways coexist (Figure 2B). We then performed a superposition of all FD curves. The superposition revealed a common pattern of predominant unfolding force peaks that best describes the mechanical unfolding pathway of hVDAC1 (Figure 3A). Each peak of this pattern corresponds to a reoccurring unfolding event toward the complete unfolding and extraction of a single hVDAC1 molecule from the lipid membrane. The unfolding intermediates identified in this way are thus common to different unfolding pathways of hVDAC1.

To assign the unfolding intermediates and reveal the average contour length (in amino acids [aa]) of the unfolded hVDAC1 polypeptide, stretched between the AFM tip and the membrane, we fitted every unfolding force peak to a worm-like-chain (WLC) model (Figures 3A and 3B). The adhesion force peaks detected at contour lengths of $\approx 1\text{--}5$ aa lay within the contact region ($\ll 5$ nm) of the tip and membrane where unspecific interactions dominate the forces detected by force spectroscopy (Oosterhelt et al., 2000; Thoma et al., 2012). These unspecific interaction forces are thus not correlated to the polypeptide sequence/structure. The analysis identified the first hVDAC1 specific force peak at a contour length of 15 ± 10 aa (average \pm SD) and the last peak at 253 ± 10 aa (Figure 3B). Although the last force peak showed a low occurrence, its existence and the fact that the preceding force peak pattern overlaps with the force peaks of all other superimposed force curves, confirmed that the force curves belong to the same unfolding pathway of the hVDAC1 channel. As demonstrated frequently, this unfolding spectrum is specific for the point of attachment of the AFM tip to the terminal end of the membrane protein and for the lipid environment, ligand binding, and functional state of the membrane protein (Bippes et al., 2013; Engel and Gaub, 2008; Ge et al., 2011; Kedrov et al., 2005; Zocher et al., 2012). The N-terminal end preceding the first β strand of the hVDAC1 barrel comprises 28 residues, while the C-terminal end following the last β strand $\beta 19$ comprises only 8 aa. From the example of various α -helical and β barrel transmembrane proteins, it has been shown that the last force peak of the unfolding force spectrum usually records the last unfolding step of a single or of grouped secondary structure elements (Oosterhelt et al., 2000; Sapra et al., 2009; Thoma et al., 2012; Zocher et al., 2012). Assuming that the AFM tip pulls hVDAC1 from the N-terminal end and that the

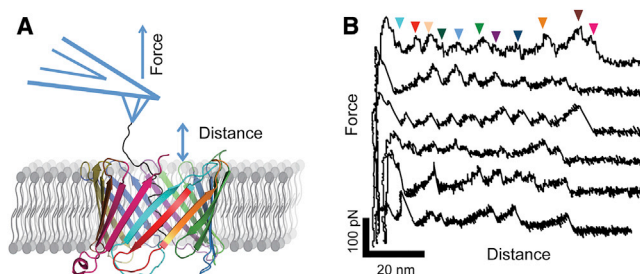


Figure 2. Mechanical Unfolding of Membrane-Embedded hVDAC1

(A) Schematics of the single-molecule force experiment. A single hVDAC1 has been non-specifically attached to the tip of an AFM cantilever. Increasing the distance of tip and membrane stretches the polypeptide bridging AFM tip and proteoliposomes. This mechanical stress establishes a force that induces the stepwise unfolding of hVDAC1.

(B) Force-distance (FD) curves recorded during unfolding show force peaks (arrowheads) that correspond to interactions established by unfolding intermediates of hVDAC1. Force variations at low distances are due to unspecific interactions, which occur in the contact area of the AFM tip and the membrane. Some FD curves lacked individual force peaks indicating missing unfolding intermediates.

last β strand β 19 will be unfolded last, then the force spectrum could extend to a contour length of at least 240 aa. If, however, the AFM tip mechanically unfolds hVDAC1 from the C-terminal end, then the force spectrum would be ≈ 20 aa shorter. Thus, only when the AFM tip preferentially attaches to the N terminus can the force peak at 253 ± 10 aa correspond to the unfolding of a transmembrane segment of hVDAC1.

On the basis of the determined contour lengths of the unfolded polypeptide stretches, we then identified the unfolding intermediates (Figures 3B and 3C): The first force peak at a contour length of 15 ± 10 aa is caused by the stretching of the flexible N-terminal domain of hVDAC1 until the α helix together with the first β strand unfold in a single step. The unfolding event releases the force causing the peak pattern in the FD curve. Subsequently, the chain is further stretched up to the next unfolding event at 40 ± 3 aa, which detects the unfolding of the β strand β 2, followed by the force peak at 57 ± 3 aa that is caused by the unfolding of β 3. All subsequent unfolding intermediates were composed of two adjacent β strands. The force peak at 253 ± 10 aa was only weakly populated, consistent with a low residual stabilization of the protein in the membrane after 17 β strands were already mechanically unfolded.

Kinetic, Conformational, and Mechanical Properties of hVDAC1

The average force detected in each unfolding step characterizes the strength of the interaction that stabilizes a structural segment (e.g., β strand or β hairpin) against unfolding (Figure 3A). On average, the unfolding of a structural segment of hVDAC1 required forces of ~ 50 – 100 pN. However, these unfolding forces depend on the loading rate, which describes the force applied by the pulling AFM tip over certain time periods (Evans and Ritchie, 1997; Janovjak et al., 2008). Probing these unfolding forces at different loading rates allows extrapolation of the lifetime, which is the reciprocal of the unfolding rate at zero force, k_0 , the transition state distance, x_u , the kinetic unfolding free energy, ΔG^\ddagger , and

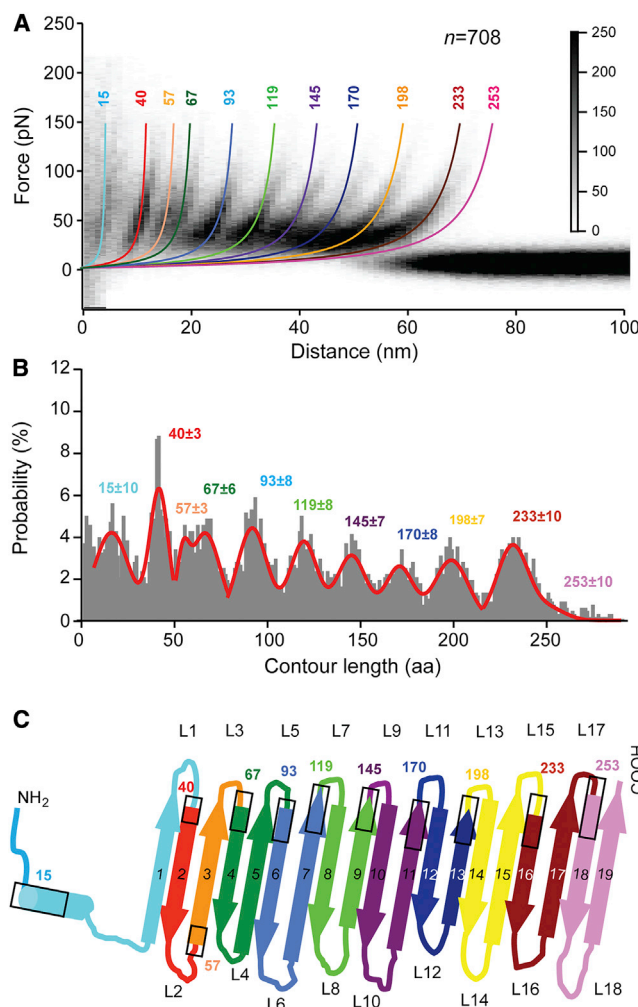


Figure 3. Unfolding Intermediates and Pathways of hVDAC1

(A) Superimposition of 708 FD curves shows the reproducibility of the FD pattern recorded upon unfolding single hVDAC1 molecules. Colored lines are worm-like chain (WLC) curves fitting individual force peaks. Numbers denote contour lengths (amino acids) of the unfolded polypeptide chain obtained from WLC fits.

(B) Probability of detecting unfolding force peaks at certain contour lengths. To obtain the histogram, every force peak of every FD curve of the superposition ($n = 708$) was fitted with the WLC model and taken into account. The most probable positions \pm SD given above each force peak were determined by multiple Gaussian fits.

(C) Average contour lengths of force peaks (position outlined by rectangles) locate structural segments of hVDAC1 (equally colored structures) that unfolded within single steps. β strands and polypeptide loops are numbered. For reproducibility of the FD pattern, see also Figure S1.

the mechanical spring constant, κ . To approach the unfolding forces at different loading rates, we unfolded hVDAC1 at velocities of 100, 300, 600, 1,200, 2,400, and 5,000 nm s⁻¹ when separating the AFM tip from the membrane (Figure S1). From these FD curves, we extracted the dynamic single-molecule force spectroscopy (DFS) plots (Experimental Procedures and Figure S2). By fitting them with the Bell-Evans model (Evans and Ritchie, 1997; Janovjak et al., 2008), we derived the parameters that describe the mechanic and kinetic properties of every

Table 1. Parameters Characterizing the Mechanical and Kinetic Properties of Membrane-Embedded hVDAC1

Peak Position/Structural Region	x_u (nm) ^a			k_0 (s ⁻¹)		
	25 mM Bis-Tris	25 mM Bis-Tris 5 mM CaCl ₂	25 mM Bis-Tris 5 mM MgCl ₂	25 mM Bis-Tris	25 mM Bis-Tris 5 mM CaCl ₂	25 mM Bis-Tris 5 mM MgCl ₂
15 aa/N terminus and β 1	0.92 \pm 0.24	0.89 \pm 0.27	0.25 \pm 0.03**	(1.8 \pm 7.9) 10 ⁻⁵	(3.1 \pm 14) 10 ⁻⁵	1.73 \pm 0.77**
40 aa/ β 2	0.78 \pm 0.14	0.34 \pm 0.05**	0.34 \pm 0.06**	(2.3 \pm 4.9) 10 ⁻³	0.44 \pm 0.40*	0.49 \pm 0.45*
57 aa/ β 3	0.86 \pm 0.06	0.48 \pm 0.06**	0.53 \pm 0.12**	(4.8 \pm 4.5) 10 ⁻⁴	0.19 \pm 0.15*	0.06 \pm 0.11
67 aa/ β 4- β 5	0.99 \pm 0.15	0.48 \pm 0.12**	0.45 \pm 0.04**	(2.2 \pm 4.6) 10 ⁻⁴	(4.4 \pm 9.2) 10 ⁻²	0.21 \pm 0.12**
93 aa/ β 6- β 7	1.25 \pm 0.25	0.83 \pm 0.28*	0.60 \pm 0.12**	(1.9 \pm 6.1) 10 ⁻⁵	(3.5 \pm 14) 10 ⁻³	0.06 \pm 0.11
119 aa/ β 8- β 9	0.56 \pm 0.04	0.49 \pm 0.02**	0.47 \pm 0.06**	(8.7 \pm 4.6) 10 ⁻²	0.19 \pm 0.06**	0.35 \pm 0.27*
145 aa/ β 10- β 11	0.94 \pm 0.10	0.80 \pm 0.17	0.45 \pm 0.09**	(3.4 \pm 4.0) 10 ⁻³	(8.3 \pm 18) 10 ⁻³	0.49 \pm 0.54*
170 aa/ β 12- β 13	0.54 \pm 0.04	0.46 \pm 0.06*	0.45 \pm 0.05**	(9.8 \pm 5.1) 10 ⁻²	0.25 \pm 0.19*	0.37 \pm 0.22*
198 aa/ β 14- β 15	0.67 \pm 0.09	0.36 \pm 0.05**	0.43 \pm 0.06**	(2.9 \pm 3.3) 10 ⁻²	1.00 \pm 0.63**	0.38 \pm 0.34*
233 aa/ β 16- β 17	0.60 \pm 0.09	0.71 \pm 0.35	0.47 \pm 0.10*	(9.2 \pm 9.4) 10 ⁻²	(3.7 \pm 14) 10 ⁻²	0.39 \pm 0.45
253 aa/ β 18- β 19	0.61 \pm 0.07	0.56 \pm 0.12	1.09 \pm 0.31**	0.52 \pm 0.34	0.92 \pm 0.91	(1.9 \pm 4.7) 10 ^{-2**}
Peak Position/Structural Region	ΔG^\ddagger (k _B T)			κ (N m ⁻¹)		
	25 mM Bis-Tris	25 mM Bis-Tris 5 mM CaCl ₂	25 mM Bis-Tris 5 mM MgCl ₂	25 mM Bis-Tris	25 mM Bis-Tris 5 mM CaCl ₂	25 mM Bis-Tris 5 mM MgCl ₂
15 aa/N terminus and β 1	31.6 \pm 4.3	31.1 \pm 4.8	20.2 \pm 0.4**	0.31 \pm 0.20	0.32 \pm 0.24	2.62 \pm 0.63**
40 aa/ β 2	26.8 \pm 2.2	21.6 \pm 0.9**	21.4 \pm 0.9**	0.36 \pm 0.16	1.56 \pm 0.56**	1.50 \pm 0.56**
57 aa/ β 3	28.4 \pm 0.9	22.4 \pm 0.8**	23.5 \pm 1.7**	0.32 \pm 0.05	0.80 \pm 0.21**	0.71 \pm 0.37*
67 aa/ β 4- β 5	29.2 \pm 2.1	23.9 \pm 2.1**	22.3 \pm 0.6**	0.25 \pm 0.09	0.85 \pm 0.50*	0.93 \pm 0.18**
93 aa/ β 6- β 7	31.6 \pm 3.3	26.4 \pm 3.9*	23.5 \pm 1.7**	0.17 \pm 0.08	0.31 \pm 0.26	0.54 \pm 0.26**
119 aa/ β 8- β 9	23.2 \pm 0.5	22.4 \pm 0.3*	21.8 \pm 0.8**	0.60 \pm 0.10	0.79 \pm 0.08**	0.81 \pm 0.23*
145 aa/ β 10- β 11	26.4 \pm 1.2	25.5 \pm 2.2	21.4 \pm 1.1**	0.25 \pm 0.06	0.33 \pm 0.17	0.86 \pm 0.37**
170 aa/ β 12- β 13	23.1 \pm 0.5	22.1 \pm 0.8*	21.7 \pm 0.6**	0.65 \pm 0.11	0.87 \pm 0.24*	0.88 \pm 0.20*
198 aa/ β 14- β 15	24.3 \pm 1.1	20.7 \pm 0.6**	21.7 \pm 0.9**	0.44 \pm 0.14	1.33 \pm 0.40**	0.99 \pm 0.34**
233 aa/ β 16- β 17	23.1 \pm 1.0	24.0 \pm 4.0	21.7 \pm 1.1	0.53 \pm 0.18	0.39 \pm 0.45	0.81 \pm 0.38
253 aa/ β 18- β 19	21.4 \pm 0.6	20.8 \pm 1.0	24.7 \pm 2.5**	0.47 \pm 0.12	0.55 \pm 0.26	0.17 \pm 0.12**

k_0 is the unfolding rate at zero force, x_u the transition state distance, ΔG^\ddagger the kinetic unfolding free energy and κ the mechanical spring constant. See also Figures S1 and S2 and Table S1.

^aParameters were obtained fitting the DFS plots (Figure S2) using Equations 1–3 (see Experimental Procedures) and present averages and SDs. Differences between hVDAC1 characterized in absence and in the presence of CaCl₂ or MgCl₂ were considered significant when p values were <0.05 (*) and <0.01 (**) from Student's t tests (Table S1) and the changes did not overlap within their SD.

structural segment of the membrane-embedded hVDAC1 channel (Table 1 and Table S1).

The width of the energy valley, which stabilizes the folded structure, can be estimated from the distance, x_u , that separates the folded and transition state toward unfolding (Figure S3). If a folded structural segment is stabilized by a wider energy valley, it can adopt more conformational states compared with a segment stabilized by a narrower energy valley (Evans and Ritchie, 1997; Janovjak et al., 2008). Widening the energy valley thus allows a structural segment to increase its conformational variability. Structural segments established by β strands and β hairpins of hVDAC1 showed transition states ranging from 0.54 to 1.25 nm (Table 1). The transition rate, k_0 , characterizing their kinetic stability, ranged from 1.8×10^{-5} to 0.52 s^{-1} and the corresponding kinetic free energy (ΔG^\ddagger) from 21.4 to 31.6 k_BT. The mechanical rigidity, κ , of individual β hairpins was as low as 0.17 N m^{-1} and reached at most 0.65 N m^{-1} .

Next, we asked how the kinetic, conformational, and mechanical properties vary for individual β strands and β hairpins of hVDAC1. Table 1 shows that the x_u values were lowest

(<0.70 nm) for β hairpins β 8- β 9, β 12- β 13, β 14- β 15, β 16- β 17, β 18- β 19 and highest (>0.90 nm) for β strand β 1 and β hairpins β 4- β 5, β 6- β 7, and β 10- β 11. In addition, κ values were lowest (<0.40 N m⁻¹) for β strands β 1, β 2, and β 3, and for β hairpins β 4- β 5, β 6- β 7, and β 10- β 11, and highest for β hairpins β 8- β 9, β 12- β 13, β 14- β 15, β 16- β 17, and β 18- β 19. Thus, the N-terminal region exposes lower mechanical rigidity and occupies a larger number of conformational states than the rest of the VDAC β barrel.

Interaction of Ca²⁺ with hVDAC1

Next we questioned whether and where Ca²⁺ interacts with hVDAC1. To localize potential Ca²⁺-binding sites in hVDAC1, we performed NMR measurements of hVDAC1 solubilized in detergent. NMR signals constitute excellent probes of complex formation (Craik and Wilce, 1997). Identification of the interaction interface is enabled by the resonance-specific assignment of the backbone signals of hVDAC1, which we had improved to 97% for the barrel residues (Villinger et al., 2010). Upon addition of increasing concentrations of Ca²⁺, amide backbone resonances

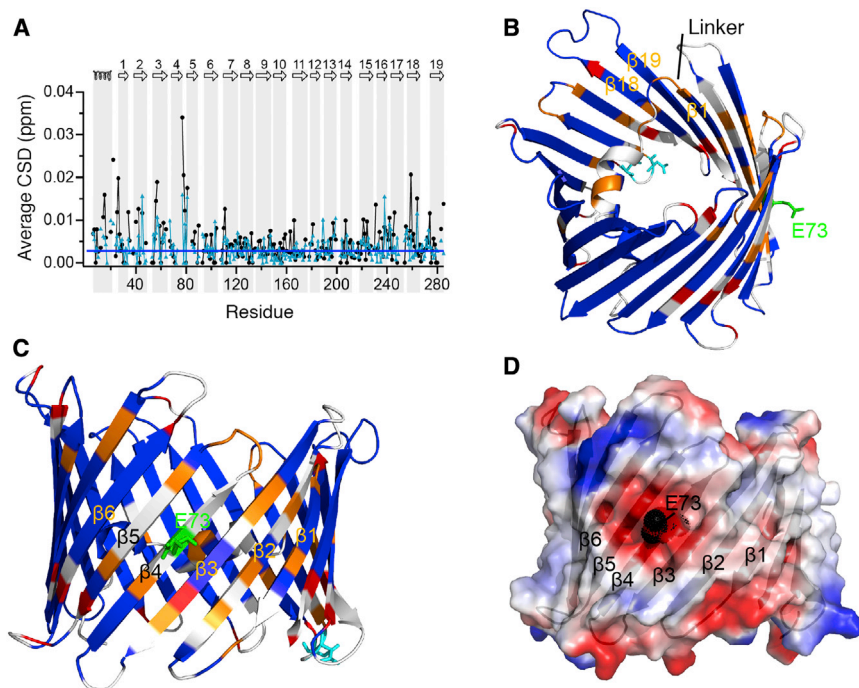


Figure 4. Binding of Ca^{2+} to hVDAC1

(A) Changes in the magnitude of ^{15}N chemical shift deviations (CSD) observed in ^1H , ^{15}N -TROSY spectra of hVDAC1 induced by a ~ 16 -fold excess of Ca^{2+} (black) and Mg^{2+} (cyan). The horizontal line indicates the average magnitude of the ^{15}N CSD threshold for non-shifting residues. The topology of hVDAC1 is shown on top.

(B and C) Residues with a magnitude of ^{15}N CSD larger than 0.05 ppm (orange) and broadening below a ratio of 0.8 (red) in (A) were mapped onto the 3D structure of mVDAC1 (PDB: 3EMN). Residues not observable or not assigned are colored white.

(D) Electrostatic potential, which was calculated in the absence of a membrane using DelPhi (Li et al., 2012), is mapped onto the surface of the hVDAC1 structure. A black sphere indicates E73.

of hVDAC1 were perturbed in a residue-specific manner in 2D ^1H , ^{15}N -transverse relaxation optimized spectroscopy (TROSY) spectra. At 16-fold excess of Ca^{2+} (corresponding to 9.6 mM Ca^{2+}), changes in peak intensities and chemical shifts were mostly localized to the N-terminal six β strands, as well as the linker, which connects the α helix to the β barrel (Figures 4A–4C). Smaller chemical shift changes occurred for residues A14 and R15 in the N-terminal α helix and the C-terminal β strands $\beta 15$ – $\beta 18$. To obtain further support for the interaction of divalent cations with the channel, we probed the influence of Mg^{2+} on the hVDAC1 spectrum (Figure 4A). Addition of 10 mM Mg^{2+} perturbed predominantly the NMR signals of residues in the six N-terminal β strands. The affected regions largely coincided with patches of negative electrostatic potential (Figure 4D).

Ca^{2+} Decreases Conformational Variability and Increases Mechanical Rigidity

Having detected that Ca^{2+} can bind to hVDAC1, we wanted to characterize whether this binding changes the energetic, kinetic, and structural properties of the channel. To this end, we performed DFS of membrane-embedded hVDAC1 in the presence of 5 mM Ca^{2+} (Figure S1). The DFS plot of every structural segment was fitted using the Bell-Evans model (Figure S2) to approximate their kinetic, energetic, and mechanical properties (Table 1). The analysis showed that addition of Ca^{2+} considerably changed the mechanical strength and flexibility, as well as the kinetic and energetic stability of hVDAC1: the x_u values, which characterize the conformational variability of hVDAC1, decreased by a factor of ~ 2 for β strands $\beta 2$ and $\beta 3$, as well as the hairpins $\beta 4$ – $\beta 5$ and $\beta 14$ – $\beta 15$. In addition, the mechanical rigidity, as reported by κ , increased in the presence of Ca^{2+} in β strand $\beta 2$ by approximately a factor of 4 and for $\beta 3$ and $\beta 14$ – $\beta 15$ by a factor of ~ 3 .

Besides the effect of Ca^{2+} on the conformational/mechanical flexibility of the hVDAC1 barrel, we found changes in the kinetic properties of individual segments (Table 1 and Table S1). For the β strands $\beta 2$ and $\beta 3$ and the β hairpin $\beta 14$ – $\beta 15$, the transition rates increased by factors of ~ 191 , ~ 395 , and ~ 34 , respectively. Because the lifetime is the reciprocal of the transition rate, these results show that the lifetime of some structural segments reduces in the presence of Ca^{2+} . In addition, the segments that showed an increased transition rate decreased their kinetic free energy by ~ 4 – $6 k_B T$.

In agreement with the NMR signal perturbation observed upon addition of Mg^{2+} , the kinetic and mechanic properties of hVDAC1 also changed in the presence of 5 mM Mg^{2+} (Table 1). Overall transition state distances decreased, transition rates increased, the unfolding free energy decreased, and the mechanical rigidity increased. Strong changes were particularly observed for the N-terminal part of the channel, as well as for β hairpins $\beta 10$ – $\beta 11$ and $\beta 14$ – $\beta 15$. In the presence of Mg^{2+} , the distance from the transition state was decreased by a factor of ~ 2 for these structural segments, the transition rate changed up to $\sim 96,000$ -fold, and the mechanical rigidity increased up to factor of ~ 8 . The Mg^{2+} -induced changes were similar to those observed for hVDAC1 in the presence of Ca^{2+} (Figure 5). However, the N-terminal domain formed by the α helix and $\beta 1$ showed the largest changes among all structural segments in the presence of Mg^{2+} .

DISCUSSION

Conformational changes determine the function of VDAC, the gatekeeper of mitochondria (Hiller and Wagner, 2009; Shoshan-Barmatz et al., 2010a; Song et al., 1998; Tejido et al., 2012; Thomas et al., 1993; Ujwal et al., 2008; Villinger et al., 2010). Little is known, however, about the nature of these structural changes, because the quantitative analysis of conformational transitions in membrane proteins when embedded into a lipid bilayer is highly challenging. To overcome these challenges, we combined single-molecule force spectroscopy with NMR

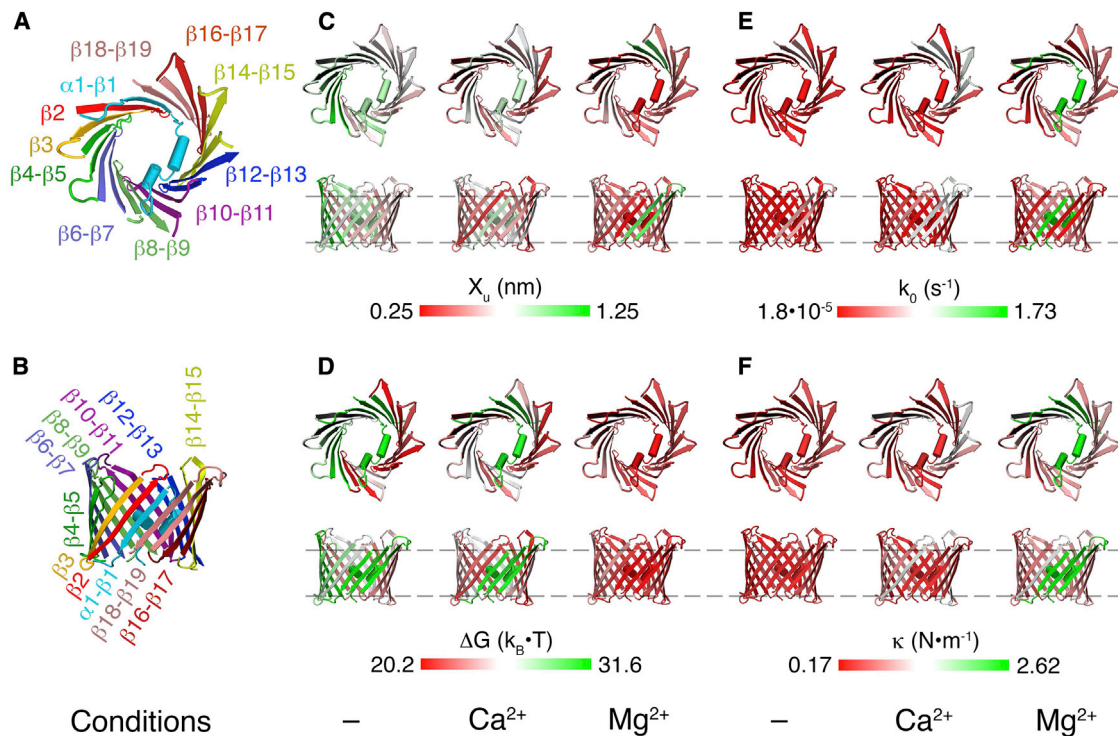


Figure 5. Kinetic, Energetic, and Mechanical Properties of Membrane-Embedded hVDAC1 in the Absence and Presence of Ca^{2+} or Mg^{2+}

(A) Top view and (B) side view of the 3D structure of hVDAC1 showing the structural segments stabilizing hVDAC1.

(C–F) Transition state distance x_u (C), free energy barrier height ΔG^\ddagger (D), transition rate k_0 (E), and spring constant κ (F) of stable structural segments in the absence (left) and presence of 5 mM Ca^{2+} (middle) or 5 mM Mg^{2+} (right). The color of the hVDAC1 backbone roughly indicates the value for each parameter as indicated by the scale bars. Values were taken from Table 1.

See also Figure S3.

measurements. Single-molecule force spectroscopy was used to quantify molecular interactions and larger interaction networks, which stabilize different functional states of single hVDAC1 channels in the absence and presence of Ca^{2+} and Mg^{2+} , while NMR spectroscopy provided complementary information about the binding of Ca^{2+} and Mg^{2+} to the hVDAC1 channel.

Our study showed that hVDAC1 preferentially unfolds via intermediates, which are composed of β hairpins (Figures 2 and 3). This stepwise unfolding is very different from the almost spontaneous force-induced unfolding of the water-soluble β barrel protein GFP (Dietz and Rief, 2004). When unfolding water-soluble proteins, the exposure of their hydrophobic core to the hydrophilic aqueous solution is one of the driving forces leading to destabilization. Thus, applying a mechanical force to initiate unfolding is often sufficient to complete their unfolding (Borgia et al., 2008). In contrast, the anisotropic environment of the lipid bilayer contributes to the structural stability of a membrane protein, so that unfolding forces must be repetitively applied until the entire protein has been unfolded (Hensen and Muller, 2013). Single-molecule force spectroscopy of membrane proteins can therefore provide access to a variety of conformational and kinetic parameters of individual membrane-embedded structural segments (Figure S3). This includes the distance x_u from the folded state to the transition state toward unfolding, which approximates the width of the energy valley that stabilizes the folded structure. Our analysis revealed that x_u values in hVDAC1

were ~30%–50% larger than those determined for α helices of most transmembrane proteins (Janovjak et al., 2008), and comparison with results for the transmembrane β barrel of OmpG suggested the same trend (Damaghi et al., 2010). In addition, we obtained quantitative information about the mechanical rigidity of the hVDAC1 channel, which is comparable with that of different transmembrane α helices (Kawamura et al., 2013; Zocher et al., 2012), but is a factor 2–10 below that of the β strands of the transmembrane β barrel protein OmpG (Damaghi et al., 2010). In addition, the superimposed force curves recorded upon unfolding of hVDAC1 (Figure 3) showed a noise, which lay above that observed upon mechanically unfolding the β barrel outer membrane proteins OmpA, OmpG, and FhuA from *Escherichia coli* (Bosshart et al., 2012; Sapra et al., 2009; Thoma et al., 2012). This noise, which indicates small variabilities among the force curves, further supports that β strands and β hairpins of hVDAC1 are structurally more variable than those of bacterial transmembrane β barrels.

Another key finding of our study is that the mechanical properties strongly vary in different parts of the hVDAC1 barrel, when the protein is incorporated into its native environment provided by the lipid bilayer (Figure 5). In particular, the N-terminal part formed by strands $\beta 1-\beta 7$ and $\beta 10-\beta 11$ showed lower mechanical rigidities and populated a higher number of conformational states. Notably, the enhanced mechanical flexibility in the N-terminal part of the liposome-embedded hVDAC1 barrel correlates

with the more flexible nature of this region when hVDAC1 was solubilized in detergent; high-resolution NMR studies showed that hydrogen/deuterium exchange is more rapid in the N-terminal part of the hVDAC1 barrel, indicating that the hydrogen bonds, which connect the β strands, are less stable (Bayrhuber et al., 2008; Villinger et al., 2010). In addition, extensive micro-to millisecond dynamics were detected in the N-terminal β strands of detergent-solubilized hVDAC1 (Bayrhuber et al., 2008; Villinger et al., 2010), consistent with a higher number of conformational states detected by single-molecule force spectroscopy. Because lipid bilayer measurements showed that several residues in the N-terminal part of the VDAC barrel are important for gating (Thomas et al., 1993), our results further suggest that a high conformational entropy and low mechanical rigidity in the N-terminal β strands play a crucial role for VDAC gating. In addition, our study highlights the potential of combining NMR spectroscopy with single-molecule force spectroscopy. While NMR spectroscopy can characterize the flexibility of membrane proteins on a wide range of timescales, particularly when solubilized in detergent, and thus provide insight into fast and slow structural processes, single-molecule force spectroscopy directly quantifies the underlying forces. As such, single-molecule force spectroscopy of membrane proteins can provide information complementary to solid-state NMR spectroscopy.

Mutation studies and photoreactive crosslinking suggested that hVDAC1 contains at least two Ca^{2+} -binding sites, which involve glutamate residues at position 73 and 203 (Israelson et al., 2007), while a Ca^{2+} ion was complexed by two E73 side chains in the asymmetric dimer in the crystal structure of mouse VDAC1 (Ujwal et al., 2008). In addition, molecular dynamics simulations and Poisson-Boltzmann calculations suggested a preferred localization of monovalent cations at the N-terminal β strands inside the pore (Choudhary et al., 2010; Rui et al., 2011). Using NMR spectroscopy, we showed that Ca^{2+} ions, as well as Mg^{2+} ions, bind with low affinity to hVDAC1 (Figure 4). In particular residues located in the N-terminal five β strands were perturbed in the presence of Ca^{2+} ions, in agreement with the observation made by single-molecule force spectroscopy that Ca^{2+} and Mg^{2+} strongly increase the mechanical flexibility of this functionally critical region of the hVDAC1 channel (Table 1). Notably, solid-state NMR spectroscopy of hVDAC1 reconstituted into liposomes has identified several structural features including the N-terminal α helix (Bauer et al., 2011; Eddy et al., 2015; Schneider et al., 2010; Zachariae et al., 2012), which is in agreement with the 3D structure of hVDAC1 determined in detergent (Bayrhuber et al., 2008; Hiller et al., 2008) and indicates that hVDAC1 embedded in the membrane exists in a properly folded conformation.

High concentrations of Ca^{2+} and Mg^{2+} strongly increased the conformational stability of the N-terminal part of the hVDAC1 channel (Figure 5). This change in the molecular plasticity can either be caused by direct binding of Ca^{2+} to the channel, as supported by NMR spectroscopy, crosslinking studies (Israelson et al., 2007), and crystallography (Ujwal et al., 2008), or be a consequence of the influence of divalent ions on the molecular properties of lipid bilayers (Pabst et al., 2007; Petrache et al., 2006). For example, localization of Ca^{2+} at the water/lipid interface (Bockmann and Grubmüller, 2004) can change the rigidity

of the lipid bilayer and thus modulate the number of conformational states sampled by hVDAC1. Notably, transient Ca^{2+} pulses with high local concentrations, so-called Ca^{2+} microdomains (Rizzuto and Pozzan, 2006), might be important, because physiological steady state concentrations of Ca^{2+} in the cytosol are in the sub-micromolar range (Bathori et al., 2006). In addition, even low Ca^{2+} concentrations can influence VDAC's molecular plasticity through Ca^{2+} -mediated dimerization (Guo et al., 1995; Hooogenboom et al., 2007; Mannella, 1982; Ujwal et al., 2008; Zalk et al., 2005). Because both mitochondrial Ca^{2+} overload and oligomerization of VDAC1 have been related to the induction of apoptosis (Crompton, 1999; Keinan et al., 2010; Shoshan-Bar-matz et al., 2010b), our data suggest a possible connection of the two mechanisms.

In summary, we showed that the molecular plasticity of human VDAC exceeds that so far observed of other transmembrane β barrel proteins, with Ca^{2+} , a key regulator of metabolism and apoptosis, strongly decreasing its plasticity. In vivo, however, other proteins such as the 18 kDa translocator protein TSPO (Gut et al., 2015; Jaremko et al., 2014), which is found in large complexes together with VDAC (Gatliff et al., 2014), might further alter the conformational variability and thus the function of VDAC.

EXPERIMENTAL PROCEDURES

Expression and Reconstitution of hVDAC1

Expression, refolding, and purification of hVDAC1 was done as previously described (Engelhardt et al., 2007). The utilized plasmid showed the insertion of three additional amino acids (RGS) between the N-terminal methionine and the second residue of the hVDAC1 sequence (final N terminus, $^1\text{MRGSAVPPTY}^{10}$) and of two amino acids (aa) at the C terminus (RS), prolonging the sequence to 288 amino acids. For better folding properties (Bayrhuber et al., 2008), a His₆-tag was present at the C terminus. For reconstitution into dimyristoylphosphatidylcholine (DMPC) liposomes, the protein was transferred into reconstitution buffer (25 mM Bis-Tris [pH 6.8], 100 mM NaCl, 0.3% lauryldimethylamine-N-oxide [LDAO]) using a desalting column. To form a lipid film, DMPC was dissolved in methanol/chloroform (1/1) and dried in a nitrogen stream followed by lyophilization to remove any organic solvents. Liposomes were generated after addition of reconstitution buffer to the film by sonication for 3 × 10 min in an ice-cooled sonication bath at 100% intensity settings. The protein in reconstitution buffer was added to the liposomes at a final protein/DMPC ratio of 1/50 (mol/mol). After incubation for 1 hr at room temperature, the detergent was removed with Calbiosorb resin (Calbiochem) at a ratio of 1 g resin/33 mg LDAO by incubation on a tilting shaker. After 5 hr of incubation, the mixture was loaded onto a sintered glass funnel. The liposomes were collected in the flow through and by washing the resin with detergent-free reconstitution buffer. The liposomes were pelleted by ultracentrifugation at 109,000 × g and washed twice with 25 mM Bis-Tris (pH 6.8). Finally the liposome pellet was re-dissolved in 25 mM Bis-Tris (pH 6.8), at a theoretical protein concentration of 1 mg ml⁻¹.

AFM Imaging

For AFM imaging, hVDAC1 membranes were adsorbed to freshly cleaved mica (≈ 30 min) in buffer solution (pH 6.8, 25 mM Bis-Tris-HCl). Loosely attached membranes were washed off with the same buffer solution. AFM topographs were recorded in the same buffer solution and at room temperature (24°C) using contact mode. To conduct AFM experiments in the presence of divalent ions, 5 mM CaCl_2 or 5 mM MgCl_2 was added to the buffer. The AFM (Nanoscope IIIe; diVeeco) was equipped with a fluid cell and oxide-sharpened Si_3N_4 cantilevers (OMCL TR400PSA; Olympus) having nominal spring constants of ≈ 0.09 N m⁻¹. High-resolution topographs were recorded at a minimal contact force of ≈ 50 –100 pN, which was manually adjusted to compensate for thermal drift (Müller and Engel, 2007). Proportional and

integral gains were adjusted to minimize the error (deflection) signal and to maximize the topographic signal. When approaching a lateral resolution of ≈ 2 nm, the scanning speed of the AFM tip was between 0.5 and $1.5 \mu\text{m s}^{-1}$. Only topographs showing identical structural features in both trace and retrace scanning directions were selected for further analysis. Topographs displaying any kind of AFM tip artifacts were not analyzed.

Single-Molecule Force Spectroscopy

After AFM-based localization of hVDAC1 in membranes, the AFM cantilever tip was pushed onto the hVDAC1 membrane applying forces ≈ 500 – 750 pN for ≈ 500 ms. Then, the AFM tip was retracted at a defined velocity (given in the figures) while recording an FD curve (Muller and Engel, 2007). FD spectra were recorded from densely packed hVDAC1 (Figure 1). For single-molecule force spectroscopy, we used $60\text{-}\mu\text{m}$ -long cantilevers (Biolevers; Olympus); spring constants ($\approx 0.03 \text{ N m}^{-1}$) were calibrated from thermal noise analysis (Butt and Jaschke, 1995) before and after each experiment. To minimize errors that may occur due to uncertainties in the cantilever spring constant calibration, hVDAC1 was unfolded using at least five different cantilevers for each pulling velocity. DFS was conducted at constant pulling velocities of 100, 300, 600, 1,200, 2,400, and $5,000 \text{ nm s}^{-1}$.

Single-Molecule Force Spectroscopy Data Selection and Analysis

In our single-molecule force spectroscopy experiments, we pushed the AFM tip onto hVDAC1 to facilitate the unspecific adhesion of the polypeptide of the protein (Muller and Engel, 2007). Thus, in principle every region of the polypeptide of hVDAC1 exposed to the AFM tip could adhere to the tip. For simplicity, we wanted to analyze only experiments that recorded the unfolding of hVDAC1 into the fully unfolded and stretched state. To reach this fully extended and unfolded state, the AFM tip must have adhered to one of the terminal ends of hVDAC1. The fully stretched hVDAC1 protein (294 residues including a His₆-tag) is ~ 106 nm long (assuming an average length of 0.36 nm per aa). For analysis, we thus automatically selected only FD curves that were >75 nm long. By this criterion, 2,168 (0.26%) out of a total of 820,649 recorded FD curves were selected for further analysis using the WLC model as described (Muller and Engel, 2007; Bippes and Muller, 2011).

Parameters characterizing the unfolding energy barrier of the structural segments that stabilize hVDAC1 were estimated from DFS plots as described (Janovjak et al., 2008). Briefly, the loading-rate (r) dependency of the most probable unfolding force (F^*) was analyzed from DFS plots using Equation 1 (Evans, 1998; Evans and Ritchie, 1997),

$$F^* = (k_B T/x_u) \ln(x_u/r/k_B T k_0), \quad (\text{Equation 1})$$

where k_B is the Boltzmann constant and T is the absolute temperature. x_u and k_0 were estimated by fitting DFS data to Equation 1 by non-linear regression. The height of the free energy barrier was estimated using the Arrhenius equation,

$$\Delta G^\ddagger = -k_B T \ln(\tau_A k_0), \quad (\text{Equation 2})$$

where the Arrhenius frequency factor $1/\tau_A$ describes the diffuse relaxation time of a structural segment. τ_A was set at 10^{-9} s (Bieri et al., 1999; Grater and Grubmüller, 2007). The mechanical spring constant of a structural segment (κ) was estimated using Equation 3 (Janovjak et al., 2008),

$$\kappa = 2\Delta G^\ddagger/x_u^2. \quad (\text{Equation 3})$$

NMR Spectroscopy

NMR spectra were recorded on samples containing 0.45 – 0.6 mM $^2\text{H}(75\%)$ - ^{15}N labeled hVDAC1 in 25 mM Bis-Tris (pH 6.8), approximately 130 mM lauryldimethylamine-oxide, and 5% – 10% (v/v) D_2O . All spectra were measured at 37°C on Bruker 800 or 900 MHz spectrometers equipped with cryogenic probes. Spectra were processed using NMRPipe (Delaglio et al., 1995) and analyzed with SPARKY (Goddard and Kneller, 2006).

Interaction of hVDAC1 with MgCl_2 and CaCl_2 was investigated by titration of hVDAC1 with the respective salt from a stock solution. $2\text{D } ^1\text{H}, ^{15}\text{N}$ -TROSY spectra (Pervushin et al., 1997) were recorded to follow ^{15}N and ^1H chemical shift changes and variations in peak intensities. Severely overlapping reso-

nances were excluded from the analysis. Normalized weighted average chemical shift deviations (CSD), $\Delta\delta_{\text{HN}}$, were calculated as

$$\Delta\delta_{\text{HN}} = \sqrt{\frac{(\Delta\delta_{\text{N}}/5)^2 + (\Delta\delta_{\text{H}})^2}{2}}, \quad (\text{Equation 4})$$

where $\Delta\delta_{\text{N}}$ and $\Delta\delta_{\text{H}}$ are the chemical shift differences for the ^{15}N and ^1H dimensions, respectively. Chemical shift and intensity changes were mapped onto the crystal structure of mVDAC1 (PDB: 3EMN) and visualized using PyMOL (DeLano, 2003). Errors in CSD were estimated by duplicate measurements of a sample with typical protein concentration and signal-to-noise ratio and are given as average values (0.014 ppm for ^{15}N CSD, 0.0028 ppm for the average CSD).

SUPPLEMENTAL INFORMATION

Supplemental Information includes three figures and one table and can be found with this article online at <http://dx.doi.org/10.1016/j.str.2016.02.012>.

AUTHOR CONTRIBUTIONS

D.J.M., M.Z., S.B., and C.G. supervised the project. S.V. performed NMR experiments and analysis. L.G., S.A.M., and D.J.M. performed AFM, single-molecule force, and DFS measurements and analysis. K.G. prepared protein samples. S.V., S.B., D.J.M., and M.Z. co-wrote the paper.

ACKNOWLEDGMENTS

This work was supported by the Max Planck Society, the Fonds der Chemischen Industrie (scholarship to S.V.), the NCCR Molecular Systems Engineering of the Swiss National Science Foundation (SNF; grant 205320_160199 to D.J.M.), and through an ERC consolidator grant to M.Z. (DYNAMOM, grant agreement no. 282008). We thank M. Damaghi for the initial single-molecule force experiments and M. Bayrhuber for the initial NMR experiments.

Received: January 8, 2016

Revised: February 12, 2016

Accepted: February 22, 2016

Published: March 24, 2016

REFERENCES

- Bathori, G., Csordas, G., Garcia-Perez, C., Davies, E., and Hajnoczky, G. (2006). Ca^{2+} -dependent control of the permeability properties of the mitochondrial outer membrane and voltage-dependent anion-selective channel (VDAC). *J. Biol. Chem.* 281, 17347–17358.
- Bauer, A.J., Gieschler, S., Lemberg, K.M., McDermott, A.E., and Stockwell, B.R. (2011). Functional model of metabolite gating by human voltage-dependent anion channel 2. *Biochemistry* 50, 3408–3410.
- Bayrhuber, M., Meins, T., Habeck, M., Becker, S., Giller, K., Villinger, S., Vonrhein, C., Griesinger, C., Zweckstetter, M., and Zeth, K. (2008). Structure of the human voltage-dependent anion channel. *Proc. Natl. Acad. Sci. USA* 105, 15370–15375.
- Benz, R. (1994). Permeation of hydrophilic solutes through mitochondrial outer membranes: review on mitochondrial porins. *Biochim. Biophys. Acta* 1197, 167–196.
- Bieri, O., Wirz, J., Hellrung, B., Schutkowski, M., Drewello, M., and Kieffhaber, T. (1999). The speed limit for protein folding measured by triplet-triplet energy transfer. *Proc. Natl. Acad. Sci. USA* 96, 9597–9601.
- Bippes, C.A., Ge, L., Meury, M., Harder, D., Ucurum, Z., Daniel, H., Fotiadis, D., and Muller, D.J. (2013). Peptide transporter DtpA has two alternate conformations, one of which is promoted by inhibitor binding. *Proc. Natl. Acad. Sci. USA* 110, E3978–E3986.
- Bippes, C., and Muller, D.J. (2011). High-resolution atomic force microscopy and spectroscopy of native membrane proteins. *Rep. Progr. Phys.* 74, 086601.
- Blachly-Dyson, E., and Forte, M. (2001). VDAC channels. *IUBMB Life* 52, 113–118.

- Bockmann, R.A., and Grubmüller, H. (2004). Multistep binding of divalent cations to phospholipid bilayers: a molecular dynamics study. *Angew. Chem. Int. Ed. Engl.* **43**, 1021–1024.
- Borgia, A., Williams, P.M., and Clarke, J. (2008). Single-molecule studies of protein folding. *Annu. Rev. Biochem.* **77**, 101–125.
- Bosshart, P.D., Iordanov, I., Garzon-Coral, C., Demange, P., Engel, A., Milon, A., and Müller, D.J. (2012). The transmembrane protein KpOmpA anchoring the outer membrane of *Klebsiella pneumoniae* unfolds and refolds in response to tensile load. *Structure* **20**, 121–127.
- Butt, H.J., and Jaschke, M. (1995). Calculation of thermal noise in atomic-force microscopy. *Nanotechnology* **6**, 1–7.
- Choudhary, O.P., Ujwal, R., Kowallis, W., Coalson, R., Abramson, J., and Grabe, M. (2010). The electrostatics of VDAC: implications for selectivity and gating. *J. Mol. Biol.* **396**, 580–592.
- Craik, D.J., and Wilce, J.A. (1997). Studies of protein-ligand interactions by NMR. *Methods Mol. Biol.* **60**, 195–232.
- Crompton, M. (1999). The mitochondrial permeability transition pore and its role in cell death. *Biochem. J.* **341** (Pt 2), 233–249.
- Damaghi, M., Sapra, K.T., Koster, S., Yildiz, O., Kuhlbrandt, W., and Müller, D.J. (2010). Dual energy landscape: the functional state of the beta-barrel outer membrane protein G molds its unfolding energy landscape. *Proteomics* **10**, 4151–4162.
- Delaglio, F., Grzesiek, S., Vuister, G.W., Zhu, G., Pfeifer, J., and Bax, A. (1995). NMRPipe: a multidimensional spectral processing system based on UNIX pipes. *J. Biomol. NMR* **6**, 277–293.
- DeLano, W.L. (2003). *PyMOL Reference Manual* (DeLano Scientific LLC).
- Dietz, H., and Rief, M. (2004). Exploring the energy landscape of GFP by single-molecule mechanical experiments. *Proc. Natl. Acad. Sci. USA* **101**, 16192–16197.
- Eddy, M.T., Ong, T.C., Clark, L., Teijido, O., van der Wel, P.C., Garces, R., Wagner, G., Rostovtseva, T.K., and Griffin, R.G. (2012). Lipid dynamics and protein-lipid interactions in 2D crystals formed with the beta-barrel integral membrane protein VDAC1. *J. Am. Chem. Soc.* **134**, 6375–6387.
- Eddy, M.T., Andreas, L., Teijido, O., Su, Y., Clark, L., Noskov, S.Y., Wagner, G., Rostovtseva, T.K., and Griffin, R.G. (2015). Magic angle spinning nuclear magnetic resonance characterization of voltage-dependent anion channel gating in two-dimensional lipid crystalline bilayers. *Biochemistry* **54**, 994–1005.
- Engel, A., and Gaub, H.E. (2008). Structure and mechanics of membrane proteins. *Annu. Rev. Biochem.* **77**, 127–148.
- Engelhardt, H., Meins, T., Poyner, M., Adams, V., Nussberger, S., Welte, W., and Zeth, K. (2007). High-level expression, refolding and probing the natural fold of the human voltage-dependent anion channel isoforms I and II. *J. Membr. Biol.* **216**, 93–105.
- Evans, E. (1998). Energy landscapes of biomolecular adhesion and receptor anchoring at interfaces explored with dynamic force spectroscopy. *Faraday Discuss.* **111**, 1–16.
- Evans, E., and Ritchie, K. (1997). Dynamic strength of molecular adhesion bonds. *Biophys. J.* **72**, 1541–1555.
- Gatliff, J., East, D., Crosby, J., Abeti, R., Harvey, R., Craigen, W., Parker, P., and Campanella, M. (2014). TSPO interacts with VDAC1 and triggers a ROS-mediated inhibition of mitochondrial quality control. *Autophagy* **10**, 2279–2296.
- Ge, L., Perez, C., Waclawska, I., Ziegler, C., and Müller, D.J. (2011). Locating an extracellular K⁺-dependent interaction site that modulates betaine-binding of the Na⁺-coupled betaine symporter BetP. *Proc. Natl. Acad. Sci. USA* **108**, E890–E898.
- Gincel, D., Zaid, H., and Shoshan-Barmatz, V. (2001). Calcium binding and translocation by the voltage-dependent anion channel: a possible regulatory mechanism in mitochondrial function. *Biochem. J.* **358**, 147–155.
- Goddard, T.D., and Kneller, D.G. (2006). *SPARKY 3* (University of California).
- Gräter, F., and Grubmüller, H. (2007). Fluctuations of primary ubiquitin folding intermediates in a force clamp. *J. Struct. Biol.* **157**, 557–569.
- Gunter, T.E., and Sheu, S.S. (2009). Characteristics and possible functions of mitochondrial Ca(2+) transport mechanisms. *Biochim. Biophys. Acta* **1787**, 1291–1308.
- Guo, X.W., and Mannella, C.A. (1993). Conformational change in the mitochondrial channel, VDAC, detected by electron cryo-microscopy. *Biophys. J.* **64**, 545–549.
- Guo, X.W., Smith, P.R., Cognon, B., D'Arcangelis, D., Dolginova, E., and Mannella, C.A. (1995). Molecular design of the voltage-dependent, anion-selective channel in the mitochondrial outer membrane. *J. Struct. Biol.* **114**, 41–59.
- Gut, P., Zweckstetter, M., and Banati, R.B. (2015). Lost in translocation: the functions of the 18-kD translocator protein. *Trends Endocrinol. Metab.* **26**, 349–356.
- Hensen, U., and Müller, D.J. (2013). Mechanistic explanation of different unfolding behaviors observed for transmembrane and soluble beta-barrel proteins. *Structure* **21**, 1317–1324.
- Hiller, S., and Wagner, G. (2009). The role of solution NMR in the structure determinations of VDAC-1 and other membrane proteins. *Curr. Opin. Struct. Biol.* **19**, 396–401.
- Hiller, S., Garces, R.G., Malia, T.J., Orekhov, V.Y., Colombini, M., and Wagner, G. (2008). Solution structure of the integral human membrane protein VDAC-1 in detergent micelles. *Science* **321**, 1206–1210.
- Hoogenboom, B.W., Suda, K., Engel, A., and Fotiadis, D. (2007). The supramolecular assemblies of voltage-dependent anion channels in the native membrane. *J. Mol. Biol.* **370**, 246–255.
- Israelson, A., Abu-Hamad, S., Zaid, H., Nahon, E., and Shoshan-Barmatz, V. (2007). Localization of the voltage-dependent anion channel-1 Ca²⁺-binding sites. *Cell Calcium* **41**, 235–244.
- Israelson, A., Zaid, H., Abu-Hamad, S., Nahon, E., and Shoshan-Barmatz, V. (2008). Mapping the ruthenium red-binding site of the voltage-dependent anion channel-1. *Cell Calcium* **43**, 196–204.
- Janovjak, H., Sapra, K.T., Kedrov, A., and Müller, D.J. (2008). From valleys to ridges: exploring the dynamic energy landscape of single membrane proteins. *Chemphyschem* **9**, 954–966.
- Jaremko, L., Jaremko, M., Giller, K., Becker, S., and Zweckstetter, M. (2014). Structure of the mitochondrial translocator protein in complex with a diagnostic ligand. *Science* **343**, 1363–1366.
- Jouaville, L.S., Pinton, P., Bastianutto, C., Rutter, G.A., and Rizzuto, R. (1999). Regulation of mitochondrial ATP synthesis by calcium: evidence for a long-term metabolic priming. *Proc. Natl. Acad. Sci. USA* **96**, 13807–13812.
- Kawamura, S., Gerstung, M., Colozo, A.T., Helenius, J., Maeda, A., Beerenwinkel, N., Park, P.S., and Müller, D.J. (2013). Kinetic, energetic, and mechanical differences between dark-state rhodopsin and opsin. *Structure* **21**, 426–437.
- Kedrov, A., Krieg, M., Ziegler, C., Kuhlbrandt, W., and Müller, D.J. (2005). Locating ligand binding and activation of a single antiporter. *EMBO Rep* **6**, 668–674.
- Keinan, N., Tyomkin, D., and Shoshan-Barmatz, V. (2010). Oligomerization of the mitochondrial protein voltage-dependent anion channel is coupled to the induction of apoptosis. *Mol. Cell Biol.* **30**, 5698–5709.
- Li, L., Li, C., Sarkar, S., Zhang, J., Witham, S., Zhang, Z., Wang, L., Smith, N., Petukh, M., and Alexov, E. (2012). DelPhi: a comprehensive suite for DelPhi software and associated resources. *BMC Biophys.* **5**, 9.
- Liu, X., Kim, C.N., Yang, J., Jemmerson, R., and Wang, X. (1996). Induction of apoptotic program in cell-free extracts: requirement for dATP and cytochrome c. *Cell* **86**, 147–157.
- Mannella, C.A. (1982). Structure of the outer mitochondrial membrane: ordered arrays of porelike subunits in outer-membrane fractions from *Neurospora crassa* mitochondria. *J. Cell Biol.* **94**, 680–687.
- McCormack, J.G., Halestrap, A.P., and Denton, R.M. (1990). Role of calcium ions in regulation of mammalian intramitochondrial metabolism. *Physiol. Rev.* **70**, 391–425.
- Müller, D.J., and Engel, A. (2007). Atomic force microscopy and spectroscopy of native membrane proteins. *Nat. Protoc.* **2**, 2191–2197.

- Narita, M., Shimizu, S., Ito, T., Chittenden, T., Lutz, R.J., Matsuda, H., and Tsujimoto, Y. (1998). Bax interacts with the permeability transition pore to induce permeability transition and cytochrome c release in isolated mitochondria. *Proc. Natl. Acad. Sci. USA* 95, 14681–14686.
- Neumann, D., Buckers, J., Kastrop, L., Hell, S.W., and Jakobs, S. (2010). Two-color STED microscopy reveals different degrees of colocalization between hexokinase-I and the three human VDAC isoforms. *PMC Biophys* 3, 4.
- Nichols, B.J., and Denton, R.M. (1995). Towards the molecular basis for the regulation of mitochondrial dehydrogenases by calcium ions. *Mol. Cell Biochem.* 149–150, 203–212.
- Oesterhelt, F., Oesterhelt, D., Pfeiffer, M., Engel, A., Gaub, H.E., and Muller, D.J. (2000). Unfolding pathways of individual bacteriorhodopsins. *Science* 288, 143–146.
- Pabst, G., Hodzic, A., Strancar, J., Danner, S., Rappolt, M., and Laggner, P. (2007). Rigidification of neutral lipid bilayers in the presence of salts. *Biophys. J.* 93, 2688–2696.
- Peng, S., Blachly-Dyson, E., Forte, M., and Colombini, M. (1992). Large scale rearrangement of protein domains is associated with voltage gating of the VDAC channel. *Biophys. J.* 62, 123–131, [discussion: 131–5].
- Pervushin, K., Riek, R., Wider, G., and Wuthrich, K. (1997). Attenuated T2 relaxation by mutual cancellation of dipole-dipole coupling and chemical shift anisotropy indicates an avenue to NMR structures of very large biological macromolecules in solution. *Proc. Natl. Acad. Sci. USA* 94, 12366–12371.
- Petrache, H.I., Zemb, T., Belloni, L., and Parsegian, V.A. (2006). Salt screening and specific ion adsorption determine neutral-lipid membrane interactions. *Proc. Natl. Acad. Sci. USA* 103, 7982–7987.
- Rizzuto, R., and Pozzan, T. (2006). Microdomains of intracellular Ca²⁺: molecular determinants and functional consequences. *Physiol. Rev.* 86, 369–408.
- Rostovtseva, T.K., Tan, W., and Colombini, M. (2005). On the role of VDAC in apoptosis: fact and fiction. *J. Bioenerg. Biomembr.* 37, 129–142.
- Rui, H., Lee, K.I., Pastor, R.W., and Im, W. (2011). Molecular dynamics studies of ion permeation in VDAC. *Biophys. J.* 100, 602–610.
- Sapra, K.T., Damaghi, M., Koster, S., Yildiz, O., Kuhlbrandt, W., and Muller, D.J. (2009). One beta hairpin after the other: exploring mechanical unfolding pathways of the transmembrane beta-barrel protein OmpG. *Angew. Chem. Int. Ed. Engl.* 48, 8306–8308.
- Schein, S.J., Colombini, M., and Finkelstein, A. (1976). Reconstitution in planar lipid bilayers of a voltage-dependent anion-selective channel obtained from paramecium mitochondria. *J. Membr. Biol.* 30, 99–120.
- Schneider, R., Etzkorn, M., Giller, K., Daebel, V., Eisfeld, J., Zweckstetter, M., Griesinger, C., Becker, S., and Lange, A. (2010). The native conformation of the human VDAC1 N terminus. *Angew. Chem. Int. Ed. Engl.* 49, 1882–1885.
- Shoshan-Barmatz, V., De Pinto, V., Zweckstetter, M., Raviv, Z., Keinan, N., and Arbel, N. (2010a). VDAC, a multi-functional mitochondrial protein regulating cell life and death. *Mol. Aspects Med.* 31, 227–285.
- Shoshan-Barmatz, V., Keinan, N., Abu-Hamad, S., Tyomkin, D., and Aram, L. (2010b). Apoptosis is regulated by the VDAC1 N-terminal region and by VDAC oligomerization: release of cytochrome c, AIF and Smac/Diablo. *Biochim. Biophys. Acta* 1797, 1281–1291.
- Song, J., Midson, C., Blachly-Dyson, E., Forte, M., and Colombini, M. (1998). The sensor regions of VDAC are translocated from within the membrane to the surface during the gating processes. *Biophys. J.* 74, 2926–2944.
- Susin, S.A., Zamzami, N., Castedo, M., Hirsch, T., Marchetti, P., Macho, A., Daugas, E., Geuskens, M., and Kroemer, G. (1996). Bcl-2 inhibits the mitochondrial release of an apoptogenic protease. *J. Exp. Med.* 184, 1331–1341.
- Szabo, I., De Pinto, V., and Zoratti, M. (1993). The mitochondrial permeability transition pore may comprise VDAC molecules. II. The electrophysiological properties of VDAC are compatible with those of the mitochondrial megachannel. *FEBS Lett.* 330, 206–210.
- Tan, W., and Colombini, M. (2007). VDAC closure increases calcium ion flux. *Biochim. Biophys. Acta* 1768, 2510–2515.
- Teijido, O., Ujwal, R., Hillerdal, C.O., Kullman, L., Rostovtseva, T.K., and Abramson, J. (2012). Affixing N-terminal alpha-helix to the wall of the voltage-dependent anion channel does not prevent its voltage gating. *J. Biol. Chem.* 287, 11437–11445.
- Territo, P.R., Mootha, V.K., French, S.A., and Balaban, R.S. (2000). Ca(2+) activation of heart mitochondrial oxidative phosphorylation: role of the F(0)/F(1)-ATPase. *Am. J. Physiol. Cell Physiol.* 278, C423–C435.
- Territo, P.R., French, S.A., Dunleavy, M.C., Evans, F.J., and Balaban, R.S. (2001). Calcium activation of heart mitochondrial oxidative phosphorylation: rapid kinetics of mVO₂, NADH, AND light scattering. *J. Biol. Chem.* 276, 2586–2599.
- Thoma, J., Bosshart, P., Pfreundschuh, M., and Muller, D.J. (2012). Out but not in: the large transmembrane beta-barrel protein FhuA unfolds but cannot refold via beta-hairpins. *Structure* 20, 2185–2190.
- Thomas, L., Blachly-Dyson, E., Colombini, M., and Forte, M. (1993). Mapping of residues forming the voltage sensor of the voltage-dependent anion-selective channel. *Proc. Natl. Acad. Sci. USA* 90, 5446–5449.
- Ujwal, R., Cascio, D., Colletier, J.P., Faham, S., Zhang, J., Toro, L., Ping, P., and Abramson, J. (2008). The crystal structure of mouse VDAC1 at 2.3 Å resolution reveals mechanistic insights into metabolite gating. *Proc. Natl. Acad. Sci. USA* 105, 17742–17747.
- Villinger, S., Briones, R., Giller, K., Zachariae, U., Lange, A., de Groot, B.L., Griesinger, C., Becker, S., and Zweckstetter, M. (2010). Functional dynamics in the voltage-dependent anion channel. *Proc. Natl. Acad. Sci. USA* 107, 22546–22551.
- Zachariae, U., Schneider, R., Briones, R., Gattin, Z., Demers, J.P., Giller, K., Maier, E., Zweckstetter, M., Griesinger, C., Becker, S., et al. (2012). beta-Barrel mobility underlies closure of the voltage-dependent anion channel. *Structure* 20, 1540–1549.
- Zalk, R., Israelson, A., Garty, E.S., Azoulay-Zohar, H., and Shoshan-Barmatz, V. (2005). Oligomeric states of the voltage-dependent anion channel and cytochrome c release from mitochondria. *Biochem. J.* 386, 73–83.
- Zimmerberg, J., and Parsegian, V.A. (1986). Polymer inaccessible volume changes during opening and closing of a voltage-dependent ionic channel. *Nature* 323, 36–39.
- Zocher, M., Zhang, C., Rasmussen, S.G., Kobilka, B.K., and Muller, D.J. (2012). Cholesterol increases kinetic, energetic, and mechanical stability of the human beta2-adrenergic receptor. *Proc. Natl. Acad. Sci. USA* 109, E3463–E3472.
- Zoratti, M., and Szabo, I. (1995). The mitochondrial permeability transition. *Biochim. Biophys. Acta* 1241, 139–176.

Structure, Volume 24

Supplemental Information

Molecular Plasticity of the Human

Voltage-Dependent Anion Channel Embedded

Into a Membrane

Lin Ge, Saskia Villinger, Stefania A. Mari, Karin Giller, Christian Griesinger, Stefan Becker, Daniel J. Müller, and Markus Zweckstetter

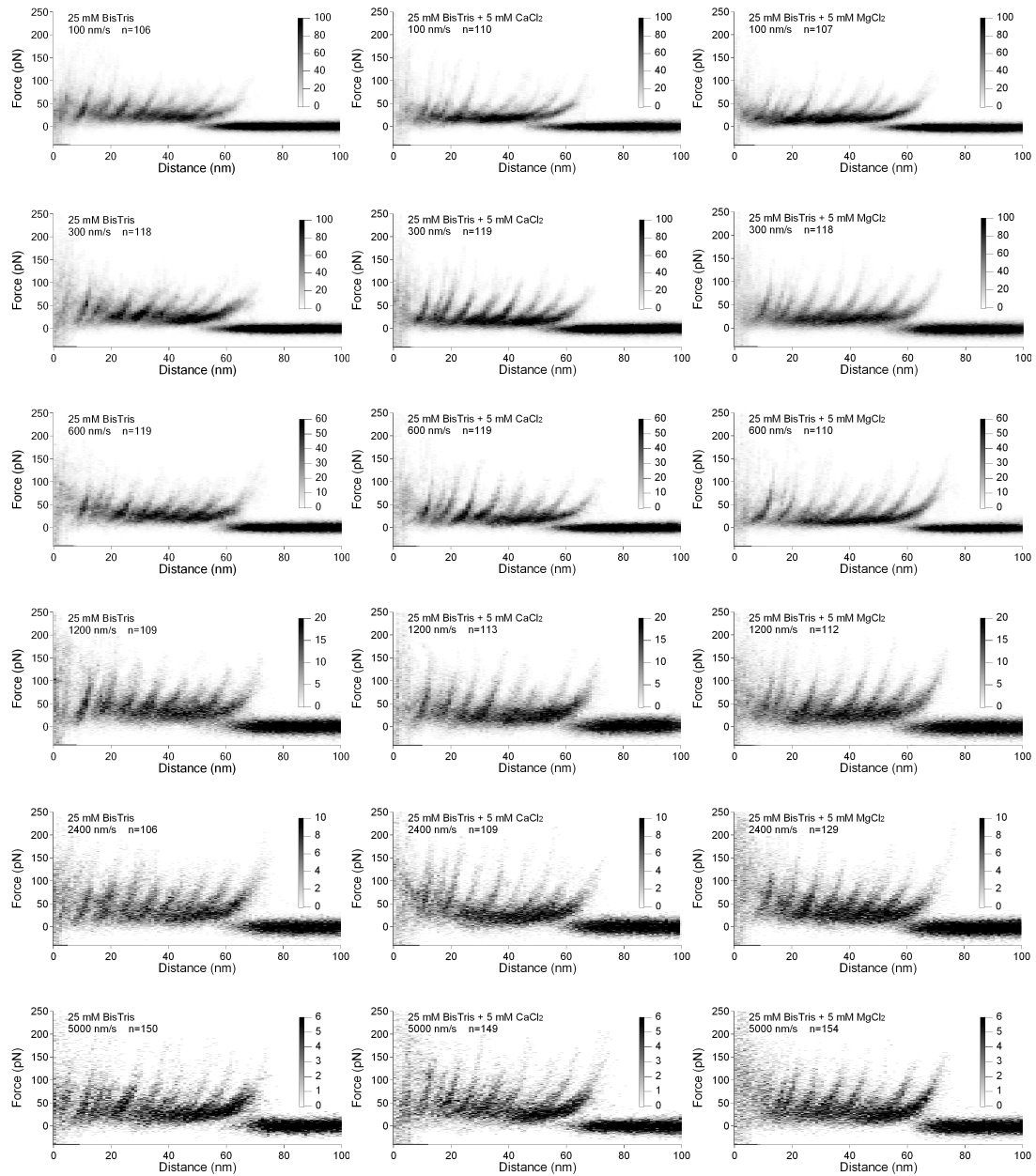


Figure S1, relates to Figure 3 and Table 1. Superimposition of FD curves recorded upon unfolding of hVDAC1 in the absence and in the presence of calcium or magnesium. Buffer conditions, pulling velocities, and number (n) of superimposed FD curves are indicated. Every superimposed FD curve has been recorded upon unfolding of a single hVDAC1 channel. The gray scale bar on the right allows the evaluation of events of high (black), lower (gray), and no (white) occurrence. Single-molecule force spectroscopy was recorded in buffer solution (25 mM BisTris, pH 6.8) and as indicated in the absence or in the presence of 5 mM Ca^{2+} or 5 mM Mg^{2+} .

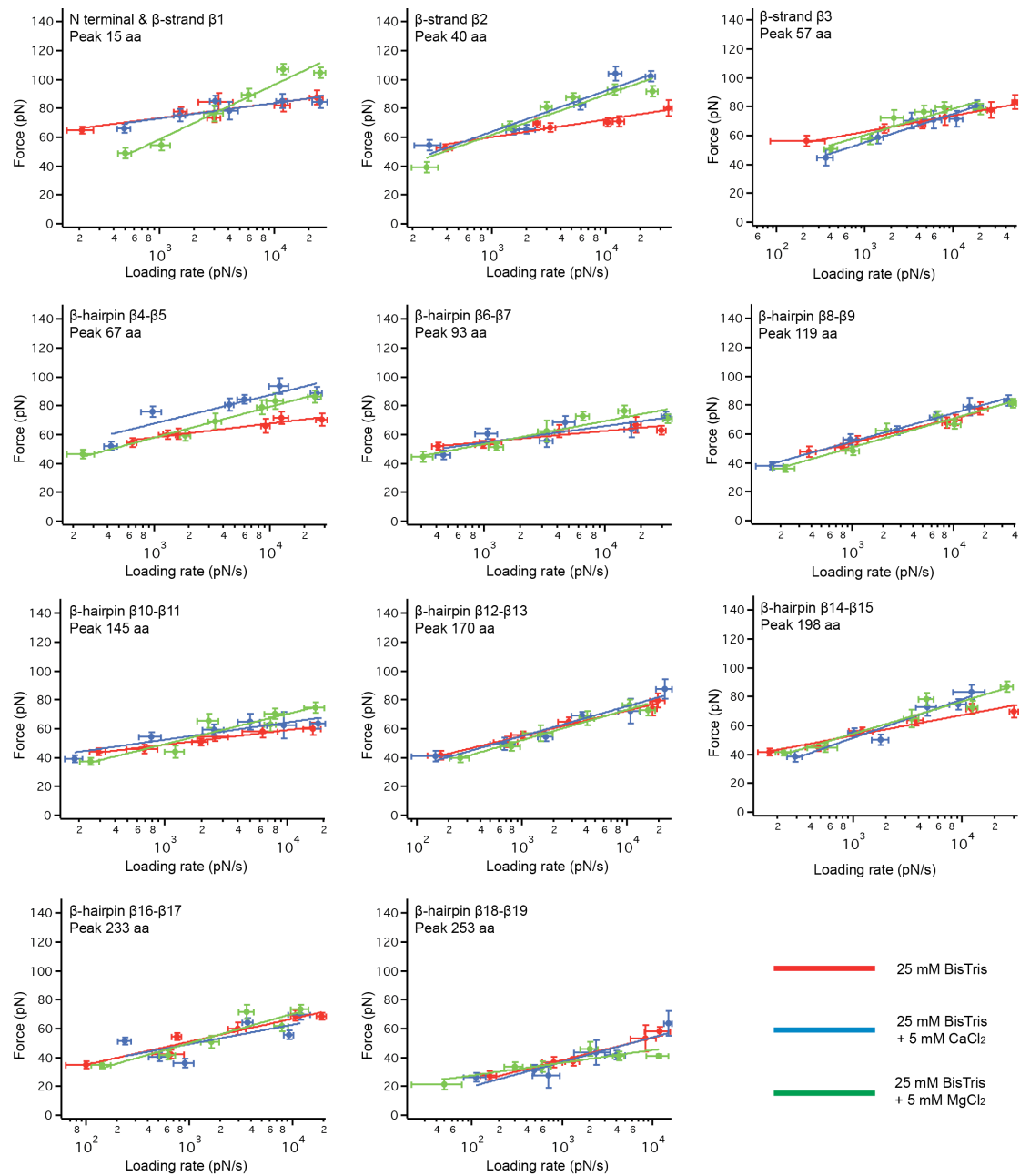


Figure S2, relates to Table 1. Dynamic single-molecule force spectroscopy (DFS) plots reveal loading rate dependent interactions stabilizing the structural segments of hVDAC1. For each stable structural segment of hVDAC1 the most probable unfolding force was determined from the raw data (**Figure S1**) and plotted against the loading rate (Experimental Procedures). The fits of the experimental data (solid lines) using Eq. 1–3 are shown for hVDAC1 unfolded in the absence of divalent ions (red), 5 mM Ca^{2+} (blue), or 5 mM Mg^{2+} (green). Values for x_u and k_0 obtained from fitting the DFS plots are given in **Table 1**. Error bars represent the standard error of most probable force and loading rate.

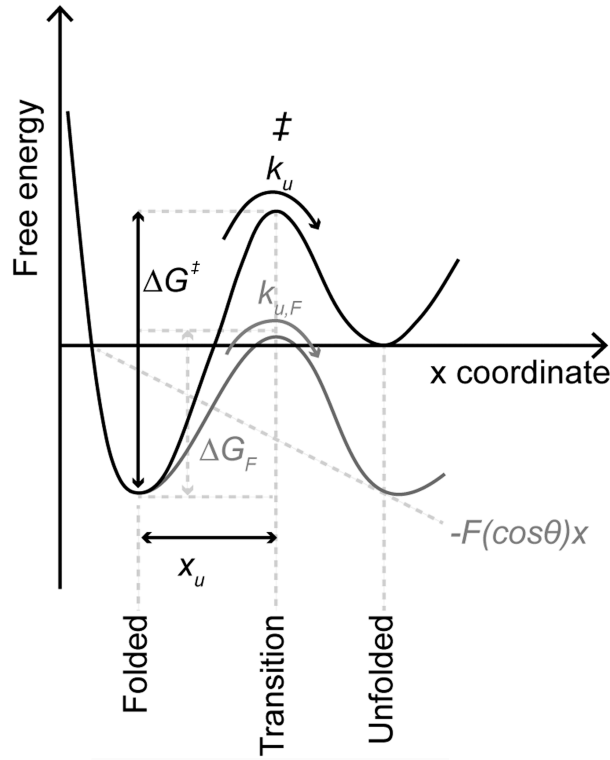


Figure S3, relates to Table 1 and Figure 5. Schematic of an energy barrier stabilizing a structural segment of hVDAC1 against unfolding. The folded state of a structural segment (e.g., for example a β -hairpin in case of hVDAC1) is separated from the unfolded state by a free energy barrier. In the absence of an externally applied force (i.e., at equilibrium) the folded structure can unfold at a certain transition rate (k_u). To unfold the structure must overcome the transition state (\ddagger). x_u characterizes the distance from the folded state to the transition state. The height of the unfolding free energy barrier separating the folded state from the unfolded state is given by ΔG^\ddagger . This barrier, which is given by the free energy difference of the folded state and the transition state, therefore characterizes the activation free energy of unfolding. According to the Bell-Evans model (Bell, 1978; Evans, 1998; Evans and Ritchie, 1997), an externally applied force (F) tilts the energy landscape by the mechanical energy ($-F(\cos\theta)x$) and lowers the free energy barrier (ΔG^\ddagger) to ΔG_F . Lowering of the free energy barrier is described by the mechanically applied pulling direction x and the angle θ of the externally applied force (F).

Table S1, relates to Table 1. Significance tests of the parameters characterizing the energy barrier parameters x_u , k_u , and ΔG^\ddagger and the spring constant κ of the stable structural segments detected for hVDAC1 in different buffer solutions. Shown are P -values revealed from T-student tests of the parameters given in Table 1.

Force peak position / Structural region	Ca ²⁺ vs control	Ca ²⁺ vs control	Ca ²⁺ vs control	Ca ²⁺ vs control
	x_u	k_u	ΔG^\ddagger	κ
15 aa / N-terminus & β 1	$8.63225 \cdot 10^{-1}$	$8.62419 \cdot 10^{-1}$	$8.51244 \cdot 10^{-1}$	$9.22322 \cdot 10^{-1}$
40 aa / β 2	$3.05692 \cdot 10^{-5}$	$2.19535 \cdot 10^{-2}$	$2.68579 \cdot 10^{-4}$	$5.3541 \cdot 10^{-4}$
57 aa / β 3	$4.34067 \cdot 10^{-7}$	$1.09213 \cdot 10^{-2}$	$2.74325 \cdot 10^{-7}$	$3.09731 \cdot 10^{-4}$
67 aa / β 4- β 5	$6.22929 \cdot 10^{-5}$	$2.69795 \cdot 10^{-1}$	$1.4011 \cdot 10^{-3}$	$1.53124 \cdot 10^{-2}$
93 aa / β 6- β 7	$2.1159 \cdot 10^{-2}$	$5.46752 \cdot 10^{-1}$	$3.0968 \cdot 10^{-2}$	$2.16478 \cdot 10^{-1}$
119 aa / β 8- β 9	$1.47059 \cdot 10^{-3}$	$7.08056 \cdot 10^{-3}$	$1.06767 \cdot 10^{-2}$	$4.99555 \cdot 10^{-3}$
145 aa / β 10- β 11	$1.04417 \cdot 10^{-1}$	$5.36127 \cdot 10^{-1}$	$4.01567 \cdot 10^{-1}$	$2.76425 \cdot 10^{-1}$
170 aa / β 12- β 13	$1.51198 \cdot 10^{-2}$	$8.58459 \cdot 10^{-2}$	$3.10518 \cdot 10^{-2}$	$7.42127 \cdot 10^{-2}$
198 aa / β 14- β 15	$1.76505 \cdot 10^{-5}$	$3.52599 \cdot 10^{-3}$	$5.28258 \cdot 10^{-5}$	$4.62344 \cdot 10^{-4}$
233 aa / β 16- β 17	$4.59109 \cdot 10^{-1}$	$4.57097 \cdot 10^{-1}$	$5.99544 \cdot 10^{-1}$	$4.92486 \cdot 10^{-1}$
253 aa / β 18- β 19	$3.77248 \cdot 10^{-1}$	$3.42859 \cdot 10^{-1}$	$2.71483 \cdot 10^{-1}$	$5.24156 \cdot 10^{-1}$

Force peak at contour length (aa)	Mg ²⁺ vs control	Mg ²⁺ vs control	Mg ²⁺ vs control	Mg ²⁺ vs control
	x_u	k_u	ΔG^\ddagger	κ
15 aa / N-terminus & β 1	$4.62349 \cdot 10^{-5}$	$2.65949 \cdot 10^{-4}$	$6.71793 \cdot 10^{-5}$	$6.15288 \cdot 10^{-6}$
40 aa / β 2	$3.58609 \cdot 10^{-5}$	$2.35747 \cdot 10^{-2}$	$2.32124 \cdot 10^{-4}$	$7.1667 \cdot 10^{-4}$
57 aa / β 3	$9.48356 \cdot 10^{-5}$	$1.94398 \cdot 10^{-1}$	$1.35225 \cdot 10^{-4}$	$2.83095 \cdot 10^{-2}$
67 aa / β 4- β 5	$4.82471 \cdot 10^{-6}$	$1.60301 \cdot 10^{-3}$	$1.69816 \cdot 10^{-5}$	$8.70332 \cdot 10^{-6}$
93 aa / β 6- β 7	$1.67672 \cdot 10^{-4}$	$1.81281 \cdot 10^{-1}$	$3.16225 \cdot 10^{-4}$	$7.60199 \cdot 10^{-3}$
119 aa / β 8- β 9	$8.89912 \cdot 10^{-3}$	$3.84503 \cdot 10^{-2}$	$4.15668 \cdot 10^{-3}$	$6.70167 \cdot 10^{-2}$
145 aa / β 10- β 11	$4.37276 \cdot 10^{-6}$	$4.88016 \cdot 10^{-2}$	$1.79251 \cdot 10^{-5}$	$2.63014 \cdot 10^{-3}$
170 aa / β 12- β 13	$4.1602 \cdot 10^{-3}$	$1.25082 \cdot 10^{-2}$	$1.7947 \cdot 10^{-3}$	$3.21037 \cdot 10^{-2}$
198 aa / β 14- β 15	$2.3926 \cdot 10^{-4}$	$2.90302 \cdot 10^{-2}$	$1.33695 \cdot 10^{-3}$	$4.25575 \cdot 10^{-3}$
233 aa / β 16- β 17	$3.60765 \cdot 10^{-2}$	$1.4135 \cdot 10^{-1}$	$4.34655 \cdot 10^{-2}$	$1.36833 \cdot 10^{-1}$
253 aa / β 18- β 19	$4.43563 \cdot 10^{-3}$	$4.46661 \cdot 10^{-3}$	$9.94509 \cdot 10^{-3}$	$1.51084 \cdot 10^{-3}$

Supplemental References

Bell, G.I. (1978). Models for the specific adhesion of cells to cells. *Science* *200*, 618-627.

Evans, E. (1998). Energy landscapes of biomolecular adhesion and receptor anchoring at interfaces explored with dynamic force spectroscopy. *Faraday Discussions* *111*, 1-16.

Evans, E., and Ritchie, K. (1997). Dynamic strength of molecular adhesion bonds. *Biophys J* *72*, 1541-1555.